Exciton and Trion Energy Transfer from Giant Semiconductor Nanocrystals to MoS₂ Monolayers

Siddharth Sampat,[†] Tianle Guo,[†] Kehao Zhang,[‡] Joshua A. Robinson,[‡] Yagnaseni Ghosh,[§]
Krishna P. Acharya,[§] Han Htoon,[§] Jennifer A. Hollingsworth,[§] Yuri N. Gartstein,[†] and Anton V. Malko*,[†]

[†]Department of Physics, The University of Texas at Dallas, Richardson, Texas 75080, United States

[‡]Department of Materials Science and Engineering, The Pennsylvania State University, University Park, Pennsylvania 16802, United States

[§]Materials Physics & Applications: Center for Integrated Nanotechnologies, Los Alamos National Laboratory, Los Alamos, New Mexico 87545, United States

ⓢ *Supporting Information*

ABSTRACT: We investigate nonradiative energy transfer (NRET) between CdSe/CdS core/shell "giant" nanocrystal quantum dots (gNQDs) and monolayer domains of molybdenum disulfide (MoS₂) grown by chemical vapor deposition. We employ three sets of gNQDs with varied core/shell parameters that exhibit radiative emission from neutral and charged excitons (trions) at different spectral positions from 590 to 660 nm as confirmed by photon statistics of individual nanocrystals. Strong photoluminescence (PL) emission quenching is observed for the donor gNQDs placed on MoS₂ domains, indicative of the efficient NRET. Analysis of the double-component PL decays reveals NRET from both neutral excitons and charged trions with the same efficiency. Applying a macroscopic electrodynamics model for the decay of electric-dipole emitters in the vicinity of an ultrathin semiconducting layer with a strong in-plane excitonic polarizability, we confirm high NRET efficiencies from >95% to 85% for dots with diameters from 10 to 20 nm. This demonstration opens new possibilities for studies of energy transfer between zero-dimensional emitters and two-dimensional absorbers, potentially enabling new avenues for multiexciton harvesting and utilization.

KEYWORDS: *TMDCs, MoS₂, giant nanocrystal quantum dots, energy transfer, trions and excitons*
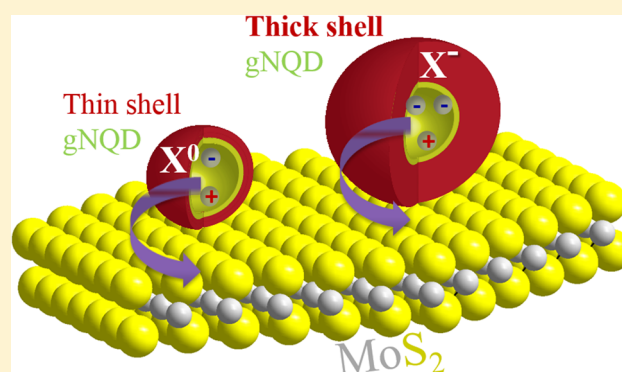
Two-dimensional (2D) transition metal dichalcogenides (TMDCs) have recently emerged as a new class of semiconducting materials featuring high charge carrier mobilities and direct optical band gaps.[1−3] Owing to the 2D confinement and reduced dielectric screening, excitons in such systems possess substantial binding energies on the order of several hundred millielectronvolts at room temperature.[4] The strong optical response makes TMDCs such as MoS₂, MoSe₂, and WS₂ good candidates for various optoelectronic applications including in photodetectors,[5] light-emitting diodes,[6] and solar-harvesting devices.

Interesting optoelectronic opportunities are associated with resonant hybrid nanostructures comprising different component materials, where energy transfer (ET) between the components is enabled by near-field electromagnetic coupling.[7] Among other things, ET-based structures aim to avoid some pitfalls of charge-transfer-based coupling by relying on longer range noncontact electromagnetic interactions. Colloidal semiconductor nanocrystal quantum dots (NQDs) have been actively explored as one of the components of such hybrids,

for instance, in hybrid NQD-on-Si architectures for solar energy conversion.[8−11] The combination of zero-dimensional (0D) NQDs with 2D TMDC materials gives a novel possibility to construct a variety of resonant 0D−2D hybrid structures, and, in fact, ET from NQDs into TDMCs has drawn both experimental[12−14] and theoretical[15] attention.

Recently developed "giant" core/shell CdSe/CdS nanocrystals (gNQDs) possess attractive photophysical properties presenting distinct advantages compared to regular nanocrystals.[16,17] In addition to size-tunable, broadband absorption and high photoluminescence quantum yield (QY), such dots are extremely photostable and nonblinking[16,18,19] and have strongly reduced rates of Auger recombination, allowing for *radiative emission* not only from ordinary excitons but also from charged and multiexciton states.[18−23] While ET from neutral exciton states commonly found in regular NQDs has been amply demonstrated, ET from higher order excited species into
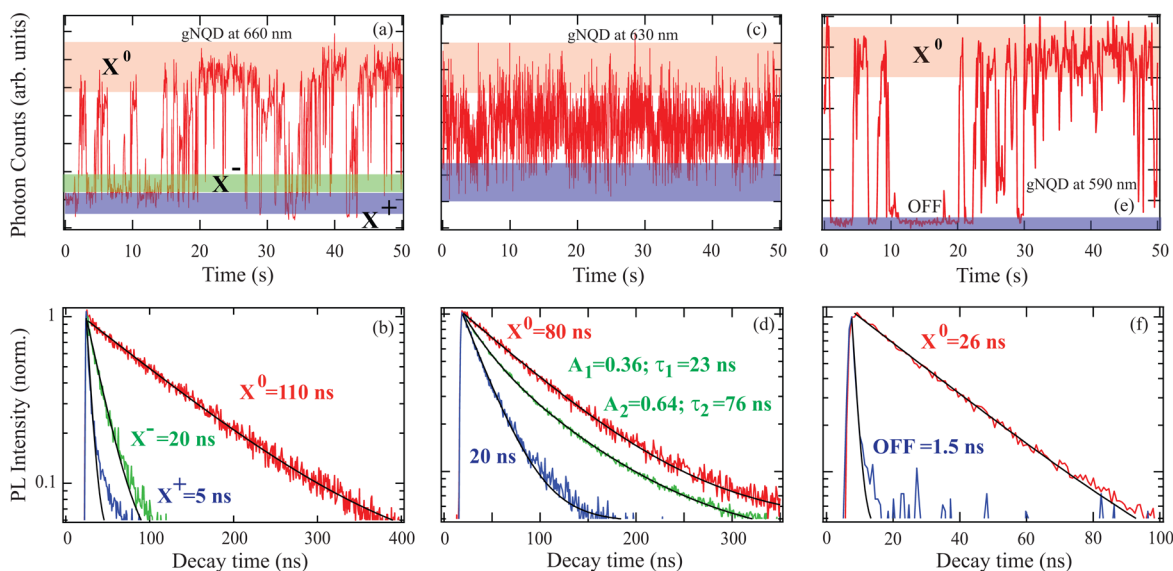
Figure 1. (a) Blinking trace and (b) extracted PL lifetimes color-coded to the shaded regions in (a) for a single large-core/large-shell gNQD emitting at 660 nm. (c, d) Same for a small-core/large-shell gNQD emitting at 630 nm. Green PL lifetime trace in (d) is compiled from all intensities in (c); red and blue PL lifetime traces are color-coded to intensity levels in (c). (e, f) Same for small-core/small-shell gNQD emitting at 590 nm.

neighboring semiconductor substrates has not been attempted yet. In this paper, we experimentally demonstrate ET from both neutral and *charged* excitons (trions) found in large-shell gNQDs into MoS_2 monolayer domains. We study three types of gNQDs with photoluminescence (PL) emission spectra peaking at 660, 630, and 590 nm. These emission lines fall into the region of energies in the vicinity of the known A and B exciton absorption peaks in monolayer MoS_2.[24] Analysis of single-dot data reveals that large-shell gNQDs (diameters ~20 nm, emission at 660 and 630 nm) have suppressed Auger rates and exhibit PL emission from neutral excitons and trions. Employing PL surface imaging, we observe substantial quenching of PL emission lifetimes for all gNQD types deposited in submonolayer assemblies on top of the MoS_2 domains, which is indicative of efficient ET. Comparison of the gNQDs' lifetime components on the reference substrate and those on MoS_2 domains shows that neutral and charged exciton species display the same acceleration of the decay due to ET into MoS_2. High ET efficiency of ~85% is estimated for these species in gNQDs emitting at 660 nm. The smaller size gNQDs (diameter ~10 nm, emission at 590 nm) exhibit only neutral exciton PL, and its decay undergoes even faster acceleration due to their closer proximity to MoS_2, with the ET efficiency estimated in excess of 95%.

We recently argued[25,26] that nonradiative ET (NRET) and excitonic PL decay of the electric-dipole emitters can be substantially affected by anisotropic dielectric properties of the nearby highly polarizable ultrathin semiconducting layers. One of the predicted polarization effects is a striking possibility of the more efficient NRET into the thinner rather than into the thicker layers, which was actually observed in the studies[12] of ET from regular NQDs into few-layer MoS_2 samples. To explain experimental ET observations, our theoretical description accommodates the polarizability of the monolayer in terms of its 2D susceptibility χ. We use the experimental optical transmittance data to assess the frequency ω dependence of the complex-valued in-plane $\chi_\parallel(\omega)$ component of susceptibility in our MoS_2 monolayers. The model calculations show good correspondence with the measured values, confirming our

prediction of efficient ET from various types of excitons. The ET coupling in hybrid structures can thus provide an effective avenue to efficiently harvest radiative charged and multiexciton species into electrically conducting substrates, potentially paving a way toward practical utilization of multicarrier states.

■ EXPERIMENTAL SECTION

Monolayer MoS_2 domains with sizes between 5 and 10 μm were prepared by chemical vapor deposition (CVD) on top of SiO_2/Si substrates with 270 nm of SiO_2 (CVD growth details given in the Supporting Information (SI)). Three sets of CdSe/CdS gNQDs with different emission wavelengths have been prepared by varying CdSe core size and CdS shell thickness using the previously described surface ionic layer adsorption and reaction (SILAR) procedure.[16,17] Dots emitting at 660 nm are composed of 5 nm diameter CdSe cores coated by 16 monolayers (MLs) of CdS shell (total diameter ~20 nm, referred to hereafter as large-core/large-shell dots); 630 nm emitting dots are composed of 2.2 nm diameter CdSe cores with 18 CdS MLs (diameter ~20 nm, small-core/large-shell dots), and 590 nm emitting dots have 2.2 nm diameter CdSe cores with 4 CdS MLs (diameter ~10 nm, small-core/small-shell dots). Nanocrystal diameters here take into account that NQDs are capped with a layer of oleic acid ligands, ensuring their solubility in nonpolar solvents and high PL QY, both in solution and on the reference glass substrates. gNQDs were deposited onto the MoS_2 domains by drop casting from 9:1 hexane/octane solution in order to form a submonolayer coverage. Scanning PL intensity and lifetime imaging was performed with an Olympus IX 71 microscope equipped with nanopositioning $x-y$ stages with a step size resolution of 50 nm. gNQDs were excited at 405 nm with 50 ps laser pulses through a 100×, 1.2 NA oil-immersion objective that is also used to collect PL. The interpulse duration was varied from 200 to 600 ns (depending on PL lifetime) in order to ensure complete relaxation of excitons between sequential laser pulses. The collected PL signal was sent to a PerkinElmer avalanche photodiode (SPCM AQR-13). Time-tagged time-correlated single photon counting (TCSPC) is performed using
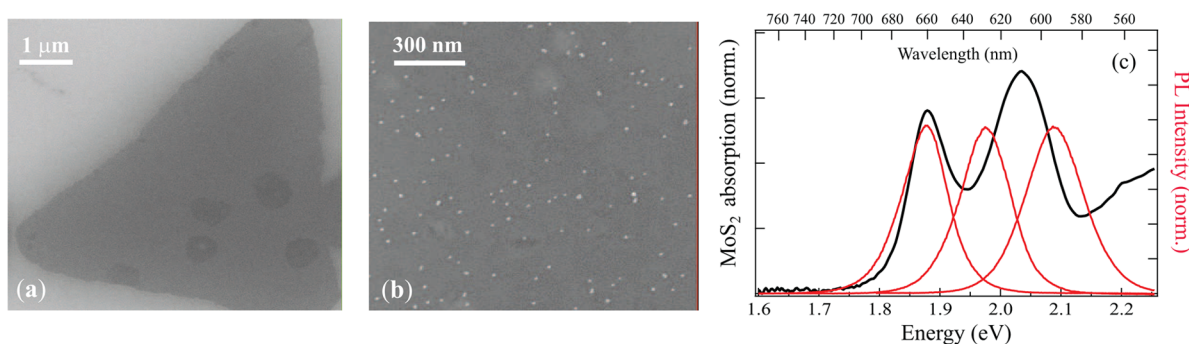
Figure 2. SEM image of CVD-grown monolayer MoS$_2$ domain (a) before and (b) after gNQD deposition. Large-core/large-shell gNQDs are seen as white dots in (b). (c) Spectral shape of the optical density of MoS$_2$ monolayer domains (black) and of the PL emission of three gNQD types (red).
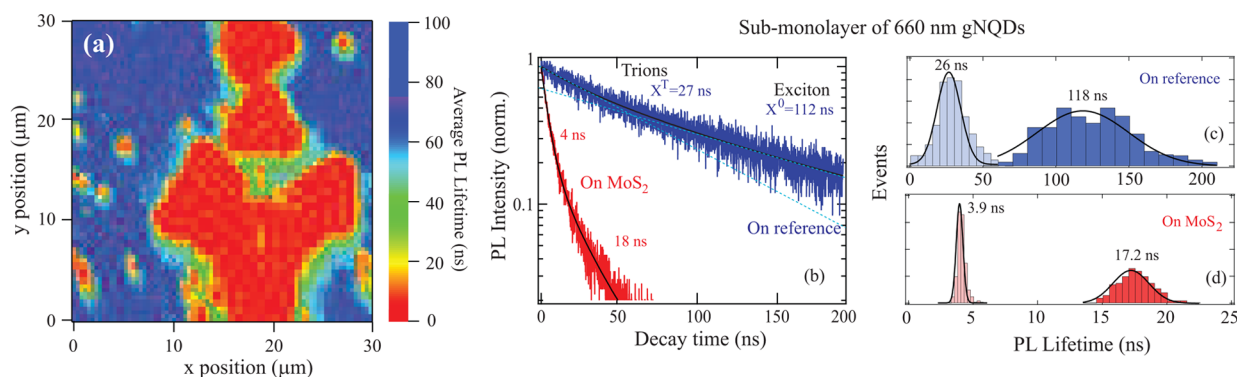
Figure 3. (a) PL lifetime surface image of several monolayer MoS$_2$ domains (red) and the reference substrate (blue) covered with large-core/large-shell gNQDs emitting at 660 nm. A good correspondence to the monolayer domain shapes in SEM images is clear. (b) Illustrative PL lifetimes of the gNQDs extracted from two positions on the PL image: red trace, PL lifetime of dots positioned on a MoS$_2$ domain; blue trace, of dots positioned on the reference substrate outside MoS$_2$ domains. Both traces are fitted with double-exponential functions with the corresponding lifetimes displayed. Dotted lines on the blue trace are guides for the eye to accentuate each of the lifetime components. (c) Lifetime distribution histograms for each of the double-exponential components compiled from reference pixels on the PL surface image shown in (a). (d) Same for locations on MoS$_2$ domains in the PL surface image. All distributions are fitted with Gaussians to determine the average lifetime values (black lines).

PicoQuant TimeHarp 200 electronics, allowing us to extract PL lifetimes of the photons recorded at any given time window. More details of the TCSPC method can be found in ref 19. The overall system time resolution was <0.5 ns, primarily defined by the detector response. During surface imaging, the step size was set at 500 nm per pixel, slightly exceeding spatial resolution of the microscope system estimated at ∼300 nm.

RESULTS

It was shown in numerous studies[18−23] that large-shell gNQDs can exhibit emission from trions and multiexcitonic complexes. Figure 1 displays representative PL emission traces (blinking traces) and extracted PL lifetimes of various emission intensity levels for individual gNQDs from each of the three samples used in this work. In agreement with the earlier studies, we observed the emergence of several low-intensity, distinct PL emission levels in the large-core/large-shell gNQD emitting at 660 nm. Analysis of the PL emission lifetimes in green- and blue-shaded intensity levels in Figure 1a,b assigns them to the emission from negatively X^- and positively charged X^+ excitons, respectively. As was previously observed, negative trions have longer PL emission lifetimes compared to positively charged ones due to the lower Auger recombination rates of these species stemming from the delocalized nature of the electronic wave function caused by small core/shell conduction band offsets.[22,23] Overall, however, the Auger rates in these dots are

sufficiently low in order to allow for the radiative recombination of trions.

Analogous data for gNQD emitting at 630 nm are shown in Figure 1c,d. The primary difference is the fast switching between the emissive states in this type of small-core/large-shell dots,[21] which precludes the appearance of the well-defined blinking levels and instead leads to the washed-out, "flickering" behavior. The PL decay extracted from the top intensity band (red-shaded region) is nevertheless well fitted with a monoexponential function, pointing to the single-exciton (X^0) behavior. The PL decay for the bottom (blue region) is also reasonably fitted with a monoexponential, the longer tail likely originating from a neutral exciton contribution. It, however, could be a superposition of X^- and X^+ emissions with similar lifetimes. This observation is supported by the PL decay compiled for all intensities (green trace in Figure 1d) that is well represented by a superposition of X^0 and trions' lifetimes. Finally, the blinking trace of the small-core/small-shell gNQD emitting at 590 nm and shown in Figure 1e,f for the most part exhibits the existence of only two well-defined intensity levels. The "ON" state represents the emission from X^0 with a PL lifetime of ∼26 ns due to a much stronger confinement of the carrier wave functions in the small volume of the dot. The completely "OFF" state possesses a very short PL lifetime of ∼1.5 ns due to the strong Auger recombination, in accordance with the previous studies.[21]
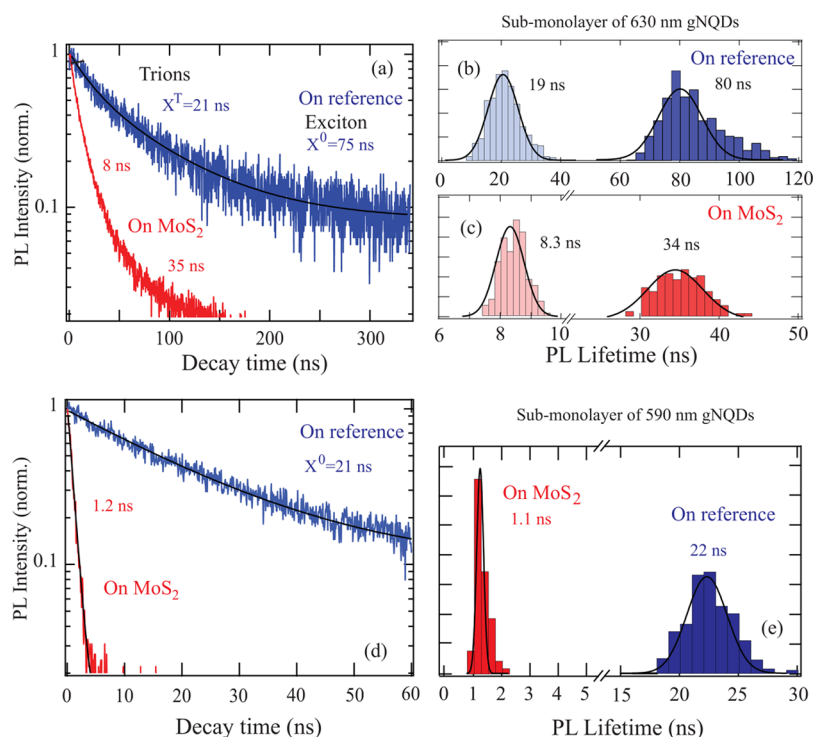
Figure 4. PL lifetime analysis of gNQDs emitting at 630 and 590 nm. (a) Representative PL decay curves on the reference substrate and on MoS$_2$ domains and (b, c) the lifetime distribution histograms using double-exponential fitting for 630 nm dots. (d, e) Same for 590 nm dots using monoexponential fitting.

In order to explore ET coupling of excitations created in giant nanocrystals, we placed gNQDs on top of the CVD-grown MoS$_2$ monolayer domains. Figure 2a and b show scanning electron microscopy (SEM) images of a monolayer MoS$_2$ domain before and after nanocrystal deposition. Despite a high PL QY of the gNQDs, we found it difficult to record the PL emission statistics from *individual* gNQDs on the MoS$_2$ monolayer due to very efficient ET that limits the number of emitted photons. Instead, we therefore used dilute gNQD solutions and deposited *submonolayers* of nanocrystals. gNQDs are placed far from each other to avoid the interactions between the dots; yet, there is a sufficient number within the excitation spot to allow for reliable PL collection. Compared to the much larger absorption cross-section and efficient PL emission of gNQDs, MoS$_2$ domains in our study were only weakly fluorescent, and their PL emission was spectrally separated; see the SI. Figure 2c compares the PL emission spectra of three gNQD types studied with the absorbance curve of MoS$_2$ that exhibits the variations in this spectral region known as due to A and B exciton peaks.[24]

Figure 3a shows the PL lifetime surface image of the submonolayer of large-core/large-shell gNQDs covering MoS$_2$ monolayer domains (red areas) and the reference SiO$_2$/Si substrate (blue areas). At each position (pixel), both PL intensity (not shown) and PL lifetimes are recorded. In this image we used monoexponential lifetime fitting to visually illustrate the strong disparity between PL lifetime values in different spatial regions. Average gNQD's PL lifetimes recorded away from domains (blue regions in Figure 3a) exhibit long decay times on the order of ~80−100 ns, similar to the native radiative lifetimes of individual gNQDs deposited on a glass surface. In contrast, PL lifetimes of gNQDs found on the top of MoS$_2$ domains even slightly away from the edges (red areas in

Figure 3a) are dramatically decreased, indicating very strong quenching of the PL due to ET into MoS$_2$.

As we discussed above, however, PL decays of this type of gNQDs are composed with contributions from neutral excitons (X^0) and charged trions (X^T). A more accurate quantitative analysis of the decay traces is exemplified in Figure 3b−d. Figure 3b shows PL decay curves extracted from two representative regions of the PL surface image. PL decay collected from a pixel within the blue region is properly fitted with a double exponential, where the longer component ($\tau_{ref}^0 = 112$ ns) is indicative of X^0 decay, while the shorter component ($\tau_{ref}^T = 27$ ns) corresponds to the decay of X^T. The histogram of statistical distributions for both components of reference PL lifetimes compiled from the blue area pixels of the PL surface scan is shown in Figure 3c, clearly delineating contributions from neutral and charged excitons. Analogously, PL decays measured in regions of MoS$_2$ domains also clearly exhibit a bimodal distribution shown in Figure 3d, whose mean values are quite smaller than the values in Figure 3c; in the example of Figure 3b, $\tau^0 = 18$ ns and $\tau^T = 4$ ns. (As the edges of the domains can have a large density of defects, the data from the yellow and green regions in Figure 3a have been excluded from the statistical analysis.)

Analyzing the decay of high-QY excitonic species, one can express their total decay rate as a sum of the decay rates into radiative and ET channels:

$$\frac{1}{\tau} = \frac{1}{\tau_{rad}} + \frac{1}{\tau_{ET}} \qquad (1)$$

yielding then ET efficiency as $\eta_{ET} = \tau/\tau_{ET}$. If we associate the decay rate measured on the reference substrate (τ_{ref}) with the radiative decay, while the total decay (eq 1) with that measured on the MoS$_2$ domains, then the transfer efficiency becomes η_{ET}

= 1 − τ/τ_{ref}. Using the central values of the bimodal distributions of the statistical histograms in Figure 3c,d—τ_{ref}^0 = 118 ns, τ^0 = 17.2 ns for neutral X^0 and τ_{ref}^T = 26 ns, τ^T = 3.9 ns for charged X^T—we find that the ratios $\tau^0/\tau_{ref}^0 \simeq \tau^T/\tau_{ref}^T$ are about the same for neutral excitons and for trions, a very meaningful result. The corresponding transfer efficiency for both species is thus estimated as $\eta_{ET} \simeq 85\%$. Given the monolayer nature of the energy acceptor MoS_2 domain and a considerable size of the energy donor gNQD, this high value of ET efficiency is impressive.

By changing the core and shell dimensions of the gNQDs, one can achieve variations of gNQD's emission wavelength, a tuning parameter to affect the spectral overlap of the donor emission and acceptor absorption. We used small-core/large-shell gNQDs to shift the peak emission wavelength to ~630 nm and small-core/small-shell dots to further shift the emission to ~590 nm, as illustrated in Figure 2c. Furthermore, by varying the core/shell dimensions, one also affects the appearance of neutral and charged excitons in the PL emission of gNQDs, which may help in gaining extra information about peculiarities of ET for different types of excitons. We recorded two more sets of PL surface scans for 630 and 590 nm emitting dots (see the SI). Figure 4a−c and Figure 4d,e show representative PL decay curves and lifetime distribution histograms for those dots, respectively. Similar to large-core/large-shell dots, small-core/large-shell dots exhibit trion emission, and PL decay curves are clearly fitted with double-exponential functions. On the contrary, PL emission from small-core/small-shells gNQDs is well fitted by monoexponential functions, indicating the absence of the trion emission. Just as in our analysis above for 660 nm dots, we find that the PL decay of 630 nm dots exhibits about the same ratios $\tau^0/\tau_{ref}^0 \simeq \tau^T/\tau_{ref}^T$ for the neutral and charged excitonic species. Using average lifetime values, the corresponding ET efficiency for 630 nm dots is thus found to be $\eta_{ET} \simeq 57\%$. Since the small-core/large-shell dots (2.2 nm core/18 ML) are approximately the same size as large-core/large-shell dots (5 nm core/16 ML), the less efficient ET found with these dots may be attributable to the reduced spectral overlap. For the small-core/small-shell dots (2.2 nm core/4 ML) emitting at 590 nm, we use the histogram data in Figure 4e for neutral excitons to arrive at a very high ET efficiency $\eta_{ET} \simeq 95\%$. Thus, in the case of much smaller size gNQDs (center-to-MoS_2 separation ~5 nm vs ~10 nm for large-shell dots), the distance dependence of ET is expected to be the major driver for the observed higher efficiency.

DISCUSSION

It is useful to discuss radiative and ET processes on the same footing as corresponding to the general electromagnetic decay of an excited species. Rate Γ (lifetime $\tau = 1/\Gamma$) of such a spontaneous decay is well recognized[27,28] to depend on the local density of electromagnetic modes, which, in turn, can be strongly affected by the environment. The macroscopic electrodynamics then provides a versatile framework to evaluate the environmental effects. This approach[28,29] was successfully applied to the spontaneous decay of various electric-dipole excitations in the vicinity of semiconducting and metallic interfaces characterized by their frequency ω-dependent dielectric functions $\varepsilon(\omega)$. Specifically, the electromagnetic decay rate Γ of the randomly oriented electric-dipole emitter in the transparent medium with dielectric constant ε_1 at distance h from the planar interface can be derived[28] as

$$\frac{\Gamma}{\Gamma_1} = 1 + \text{Re} \int_0^\infty \frac{k_\parallel dk_\parallel}{2k_1 k_{1z}} f(k_\parallel) \tag{2}$$

where Γ_1 is the spontaneous radiative decay rate this emitter would have in the uniform medium with dielectric constant ε_1, $k_1^2 = \varepsilon_1 k_0^2$, $k_{1z}^2 = k_1^2 - k_\parallel^2$ for wave vectors and their components, and

$$f(k_\parallel) = [(2k_\parallel^2/k_1^2 - 1)r^{(p)} + r^{(s)}]e^{2ik_{1z}h} \tag{3}$$

The integration variable $k_\parallel$ in expression 2 has the meaning of the in-plane (parallel to the interface) component of the wave vector, whose scale is compared to the vacuum wavenumber $k_0(\omega) = \omega/c$. The effect of the interface is contained in eq 3 via the reflection coefficient amplitudes $r^{(p)}$ and $r^{(s)}$ for respectively p- and s-polarized waves. We reiterate that eq 2 naturally includes modifications of the decay rate of both a radiative nature and a nonradiative nature as determined by the properties of and the distance to the interface (substrate).

In our experiments, we compare decay rates in two different configurations: on the reference substrate, which we denote Γ_{ref}, and then on the substrate with a MoS_2 monolayer, denoted Γ_{MoS_2}. It is the modification *ratio* $\Gamma_{MoS_2}/\Gamma_{ref}$ of the decay rates in the two configurations that is of interest to us here, which is also underlined by eq 2. While the absolute magnitude of Γ, of course, significantly depends on the emitter itself, the ratio is rather determined by the emitter's environments (generalized Purcell effect[30,31]). These considerations provide a proper perspective on our experimental observation of nearly the same modification ratios found for PL lifetimes of neutral excitons and of trions. It should also be emphasized that such ratios are robust with respect to the size of the emitting exciton wave function as long as the wave function is spherically symmetric,[31] thus enabling the point electric-dipole framework for calculations of the modification of decay rates for excited states in spherical NQDs of variable sizes.

The purpose of our discussion here is to provide an unobscured illustration of the expected magnitude and some important drivers of the ET process. To this end, we consider a simpler familiar model of a planar interface between two (nonmagnetic) media with dielectric constants ε_1 and ε_2. For the reference configuration, the reflection amplitudes are then given just by standard textbook expressions.[28] A convenient practical way to take account of the monolayer in the macroscopic electrodynamics is to treat it as an infinitesimally thin layer at the interface characterized by the two-dimensional susceptibility χ that determines the polarization response to the electric field.[15,32] Generally, this susceptibility is anisotropic with its in-plane, $\chi_\parallel$, and out-of-plane, $\chi_\perp$, components. (If compared to an anisotropic macroscopic layer of thickness d, those components can be associated with $(\varepsilon_\parallel - 1)d$ and $(1 - 1/\varepsilon_\perp)d$, respectively.) For the range of frequencies in this study ($\hbar\omega$ around 2 eV), it is the in-plane susceptibility $\chi_\parallel$ of MoS_2 that plays the major role. Its effect on the reflection amplitudes is derived[15] with the boundary conditions of the polarizable interface monolayer as

$$r^{(p)} = \left(\frac{\varepsilon_2}{k_{2z}} - \frac{\varepsilon_1}{k_{1z}} - i\chi_\parallel\right)\left(\frac{\varepsilon_2}{k_{2z}} + \frac{\varepsilon_1}{k_{1z}} - i\chi_\parallel\right)^{-1} \tag{4}$$

and

$$r^{(s)} = (k_{1z} - k_{2z} + ik_0^2\chi_\parallel)(k_{1z} + k_{2z} - ik_0^2\chi_\parallel)^{-1} \tag{5}$$
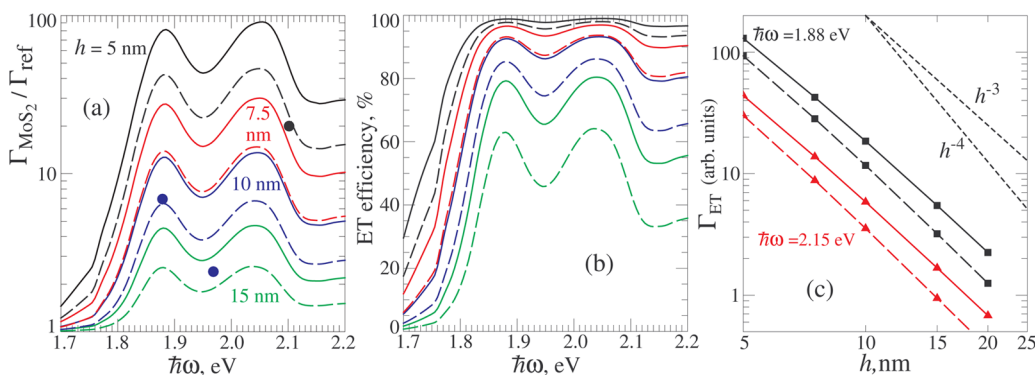
Figure 5. (a) ω-Dependent acceleration of decay rates (eq 2) due to the MoS$_2$ monolayer for a randomly oriented electric-dipole exciton transition for different distances h to the interface. Solid lines show the results derived for $\varepsilon_2 = 2.25$ and dashed lines for $\varepsilon_2 = 4$. To compare, circular dots display the experimental ratios we discussed above for gNQDs at 660, 630, and 590 nm emission wavelengths. Dots are color-coded for the approximate matching to the distance-dependent curves. (b) Calculated ET efficiency into the MoS$_2$ monolayer, eq 9, as corresponding and color-matched to the results in panel (a) complemented by the evaluation of the radiative rates (eq 6). (c) Distance dependence of ET rates extracted from the calculated data at two transition frequencies: data points connected with solid lines are for $\varepsilon_2 = 2.25$ and with dashed lines for $\varepsilon_2 = 4$. Short-dashed lines are guides to the eye to indicate the slopes corresponding to the $1/h^4$ and $1/h^3$ scaling.

[Formulas 4 and 5 reduce to the familiar[28] interface reflection coefficients upon $\chi_\| = 0$. With account of $\chi_\perp$, expressions 4 and 7 become more involved; see the SI for illustrations of the effects of $\chi_\perp$.]

As noted above, decay rate (eq 2) describes all electromagnetic decay channels including the radiative decay into photons propagating through the transparent media sandwiching in our model the MoS$_2$ monolayer. The rate of this radiative decay can be written[28] as

$$\frac{\Gamma_{\text{rad}}}{\Gamma_1} = \frac{1}{2} + \int_0^{k_1} \frac{k_\| dk_\|}{4 k_1 k_{1z}} [|r^{(p)}|^2 + |r^{(s)}|^2 + 2\text{Re}f(k_\|)]$$
$$+ \int_0^{k_2} \frac{k_{2z} k_\| dk_\|}{4 k_1 |k_{1z}|^2} \left[\frac{k_\|^2 + |k_{1z}|^2}{k_1^2} |t^{(p)}|^2 + |t^{(s)}|^2 \right] e^{-2\text{Im}k_{1z}h} \tag{6}$$

where $k_2^2 = \varepsilon_2 k_0^2$ and $k_{2z}^2 = k_2^2 - k_\|^2$ refer to the wave vectors in the medium with ε_2. The monolayer's $\chi_\|$ affects the familiar[28] transmission coefficient amplitudes in correspondence with the reflection coefficients (eqs 4 and 5):

$$t^{(p)} = 2 \frac{\sqrt{\varepsilon_1 \varepsilon_2}}{k_{2z}} \left(\frac{\varepsilon_2}{k_{2z}} + \frac{\varepsilon_1}{k_{1z}} - i\chi_\| \right)^{-1} \tag{7}$$

and

$$t^{(s)} = 2 k_{1z} (k_{1z} + k_{2z} - i k_0^2 \chi_\|)^{-1} \tag{8}$$

Calculating decay rates in eqs 2 and 6 allows one to evaluate the modification of the NQD emitter's lifetime due to the presence of the monolayer as well as to assess the efficiency η of ET into the monolayer:

$$\eta = \Gamma_{\text{ET}}/\Gamma_{\text{MoS}_2}, \qquad \Gamma_{\text{ET}} = \Gamma_{\text{MoS}_2} - \Gamma_{\text{rad}} \tag{9}$$

Our numerical examples in Figure 5 are computed for the first medium as air ($\varepsilon_1 = 1$) and two cases of the second medium: (1) $\varepsilon_2 = 2.25$ as appropriate for the system we studied experimentally and (2) somewhat larger $\varepsilon_2 = 4$, to assess the effect of the substrate polarizability. To accomplish the calculations, one, of course, needs to know the monolayer's susceptibility χ. The frequency dependence of this complex-valued quantity, $\chi(\omega) = \chi'(\omega) + i\chi''(\omega)$, is particularly relevant

for our application and realistically accessible from optical measurements. The absorption measurements are usually used to address the imaginary part of the response, while the spectroscopic ellipsometry is a powerful tool to deduce both real and imaginary parts. Some helpful ellipsometric measurements of monolayer and thin-film MoS$_2$ samples are available in the literature;[33,34] they, however, were not analyzed in terms of the anisotropic response functions. Here we use $\chi_\|(\omega)$ approximately deduced from our own transmittance measurements (see the SI for details on the real and imaginary parts of the response).

We evaluate eqs 2 and 6 in the spectral region of excitonic resonances using eqs 4, 5, 7, and 8, with the results displayed in Figure 5. Panel (a) of this figure clearly illustrates the effects of transition frequency ω, distance h, and the polarizability of the substrate (ε_2) on the acceleration of the spontaneous electromagnetic decay rate in the presence of the MoS$_2$ monolayer. It is evident that the relative magnitudes of the acceleration decrease for a more polarizable substrate. This is a consequence of a larger screening by the substrate of the ET-enabling electric field in the vicinity of the monolayer. The electrostatic effects of the substrate on the related dispersion of the exciton-polaritons in monolayers have been noted before.[15] For comparison, the panel also shows three experimental data points corresponding to the acceleration of the average decay rates reported in Figures 3 and 4. Experimental points, color-coded to the modeled curves in Figure 5a, correspond well to the exhibited trends especially since no fitting parameters were used in calculations. Still, the absolute values of the computational data obtained for the $\varepsilon_2 = 2.25$ substrate (glass) are higher than the shown experimental points. One of the likely sources of this difference is an approximate character of susceptibility χ used in model calculations, which could also be affected by a nonuniformity of studied samples as well as possible variations of the distance from NQD centers to the interface. More detailed comparisons will become possible as an accurate characterization of the response functions of uniform monolayer samples is made available.

Figure 5b illustrates high efficiencies (eq 9) achievable for ET from NQDs into the monolayer even from appreciable distances in excess of 10 nm. Computations explicitly show (see the SI) that modifications of purely radiative decay rates

(eq 6) in the presence of a MoS_2 monolayer are relatively very insignificant so that the substantial changes in the total decay rate $\Gamma_{MoS_2}/\Gamma_{rad}$ observed experimentally are caused by ET into the monolayer (this validates the simple analysis with eq 1). A more quantitative view at the distance h dependence of ET is shown in the double-logarithmic plot of Figure 5c, where the computed data clearly exhibit the distance falloff of Γ_{ET} slower than the traditionally[27,29,35] assumed $1/h^4$ scaling for NRET into thin layers. As we discussed recently,[25] the $1/h^4$ scaling for Förster-like NRET is appropriate for energy acceptor layers with additive ET rates, that is, for weakly interacting energy acceptor systems. In the case of strongly interacting acceptor dipoles, their mutual polarization leads to nonadditivity and plays an important role in the resulting behavior. MoS_2 layers with their large in-plane polarizability is a good example[12] of such systems, where the strong polarization response is accompanied by a slower distance falloff, exhibited in Figure 5c. It is interesting to note that a still different distance (and frequency) dependence of ET into the monolayer is possible if the excitonic absorption lines were much narrower than in our current samples. In this case ET would correspond to the excitation of coherent exciton-polaritons in the monolayer,[15] conceptually similar to the excitation of surface plasmons.[29] Low-temperature studies of ET into defect-free monolayer samples are needed to verify if such an intrinsic behavior is achievable.

CONCLUSIONS

In summary, we used three types of giant core/shell nanocrystals (gNQDs) that exhibit *neutral* and *charged* radiative excitonic states to demonstrate that *both* excited species can efficiently transfer their energy into a neighboring 2D semiconductor substrate. PL surface scanning reveals a substantial acceleration of PL decay for gNQD energy donors on top of the CVD-grown monolayer MoS_2 domains. Analysis of the PL lifetime components shows the same ET transfer efficiencies for both types of excitonic species, in agreement with the expected effect of the environment on spontaneous electromagnetic decay rates. The experimental results are supported by an electrodynamics model that describes the decay rate of an electric-dipole emitter in the vicinity of a TMDC interfacial layer with a strong excitonic polarization response along the layer. Computations confirm that high ET efficiencies in excess of 80% and 90% can be achieved depending on the gNQD size.

The experimental observation of the efficient ET coupling between various excitonic species in core/shell gNQDs and ultrathin semiconductor materials indicates potential for creation of hybrid architectures that would operate with higher order multiexciton (MX) complexes. The prospect of MX harvesting via ET coupling may, for instance, open interesting opportunities in photovoltaics. Modern nanocrystal-based solar cells are not used in solar concentrator/high solar flux geometries due to the Auger recombination preventing long-lived higher order excitons. Using robust and photostable giant nanocrystals with suppressed Auger recombination rates combined with efficient ET of MXs might allow increasing the conversion efficiencies beyond the one-sun illumination limits. Further, ET schemes might benefit harvesting of MXs generated via multicarrier generation mechanisms, broadly thought to alleviate carrier thermalization losses.

ASSOCIATED CONTENT

Ⓢ Supporting Information

The Supporting Information is available free of charge on the ACS Publications website at DOI: 10.1021/acsphotonics.6b00088.

Additional information (PDF)

AUTHOR INFORMATION

Corresponding Author
*E-mail: anton.malko@utdallas.edu.
Notes
The authors declare no competing financial interest.

ACKNOWLEDGMENTS

REFERENCES

(1) Mak, K.; Lee, C.; Hone, J.; Shan, J.; Heintz, T. Atomically thin MoS_2: a new direct-gap semiconductor. *Phys. Rev. Lett.* **2010**, *105*, 2−5.

(2) Splendiani, A.; Sun, L.; Zhang, Y.; Li, T.; Kim, J.; Chim, C.-Y.; Galli, G.; Wang, F. Emerging photoluminescence in monolayer MoS_2. *Nano Lett.* **2010**, *10*, 1271−1275.

(3) Rao, C. N. R.; Maitra, U.; Waghmare, U. V. Extraordinary attributes of 2-dimensional MoS_2 nanosheets. *Chem. Phys. Lett.* **2014**, *609*, 172−183.

(4) Yu, H.; Cui, X.; Xu, X.; Yao, W. Valley excitons in two-dimensional semiconductors. *Natl. Sci. Rev.* **2015**, *2*, 57.

(5) Kufer, D.; Nikitskiy, I.; Lasanta, T.; Navikaite, G.; Koppens, F. H. L.; Konstantatos, G. Hybrid 2D/0D MoS_2/PbS Quantum Dot Photodetectors. *Adv. Mater.* **2015**, *27*, 176−180.

(6) Sundaram, R. S.; Engel, M.; Lombardo, A.; Krupke, R.; Ferrari, A. C.; Avouris, P.; Steiner, M. Electroluminescence in Single Layer MoS_2. *Nano Lett.* **2013**, *13*, 1416−1421.

(7) Agranovich, V. M.; Gartstein, Y. N.; Litinskaya, M. Hybrid Resonant Organic-Inorganic Nanostructures for Optoelectronic Applications. *Chem. Rev.* **2011**, *111*, 5179−5214.

(8) Nguyen, H. M.; Seitz, O.; Aureau, D.; Sra, A.; Nijem, N.; Gartstein, Y. N.; Chabal, Y. J.; Malko, A. V. Spectroscopic Evidence for Nonradiative Energy Transfer between Colloidal CdSe/ZnS Nanocrystals and Functionalized Silicon Substrates. *Appl. Phys. Lett.* **2011**, *98*, 161904−3.

(9) Nguyen, H. M.; Seitz, O.; Peng, W.; Gartstein, Y. N.; Chabal, Y. J.; Malko, A. V. Efficient Radiative and Nonradiative Energy Transfer from Proximal CdSe/ZnS Nanocrystals into Silicon Nanomembranes. *ACS Nano* **2012**, *6*, 5574−5582.

(10) Nimmo, M. T.; Caillard, L. M.; De Benedetti, W.; Nguyen, H. M.; Seitz, O.; Gartstein, Y. N.; Chabal, Y. J.; Malko, A. V. Visible to Near-Infrared Sensitization of Silicon Substrates via Energy Transfer from Proximal Nanocrystals: Further Insights for Hybrid Photovoltaics. *ACS Nano* **2013**, *7*, 3236−3245.

(11) Peng, W.; Rupich, S. M.; Shafiq, N.; Gartstein, Y. N.; Malko, A. V.; Chabal, Y. J. Silicon Surface Modification and Characterization for Emergent Photovoltaic Applications Based on Energy Transfer. *Chem. Rev.* **2015**, *115*, 12764−12796.

(12) Prins, F.; Goodman, A. J.; Tisdale, W. A. Reduced dielectric screening and enhanced energy transfer in single- and few-layer MoS_2. *Nano Lett.* **2014**, *14*, 6087−6091.

(13) Prasai, D.; Klots, A. R.; Newaz, A.; Niezgoda, J. S.; Orfield, N. J.; Escobar, C. A.; Wynn, A.; Efimov, A.; Jennings, G. K.; Rosenthal, S. J.; Bolotin, K. I. Electrical Control of near-Field Energy Transfer between Quantum Dots and Two-Dimensional Semiconductors. *Nano Lett.* **2015**, *15*, 4374.

(14) Goodfellow, K. M.; Chakraborty, C.; Sowers, K.; Waduge, P.; Wanunu, M.; Krauss, T.; Driscoll, K.; Vamivakas, A. N. Distance-dependent energy transfer between CdSe/CdS quantum dots and a two-dimensional semiconductor. *Appl. Phys. Lett.* **2016**, *108*, 021101.

(15) Gartstein, Y. N.; Li, X.; Zhang, C. Exciton polaritons in transition-metal dichalcogenides and their direct excitation via energy transfer. *Phys. Rev. B: Condens. Matter Mater. Phys.* **2015**, *92*, 075445.

(16) Chen, Y.; Vela, J.; Htoon, H.; Casson, J. L.; Werder, D. J.; Bussian, D. A.; Klimov, V. I.; Hollingsworth, J. A. Giant" Multishell CdSe Nanocrystal Quantum Dots with Suppressed Blinking. *J. Am. Chem. Soc.* **2008**, *130*, 5026−5027.

(17) Hollingsworth, J. A. Heterostructuring Nanocrystal Quantum Dots: Toward Intentional Suppression of Blinking and Auger Recombination. *Chem. Mater.* **2013**, *25*, 1318−1331.

(18) Htoon, H.; Malko, A. V.; Bussian, D.; Vela, J.; Hollingsworth, J. A.; Chen, Y.; Klimov, V. I. Highly Emissive Multiexcitons in Steady-State Photoluminescence of Individual "Giant" CdSe/CdS Core/Shell Nanocrystals. *Nano Lett.* **2010**, *10*, 2401−2407.

(19) Malko, A. V.; Park, Y.-S.; Sampat, S.; Vela, J.; Chen, Y.; Hollingsworth, J. A.; Klimov, V. I.; Htoon, H. Pump-Intensity- and Shell-Thickness-Dependent Evolution of Photoluminescence Blinking in Individual Core/Shell CdSe/CdS Nanocrystals. *Nano Lett.* **2011**, *11*, 5213−5218.

(20) Park, Y.-S.; Malko, A. V.; Vela, J.; Ghosh, Y.; Garcia-Santamaria, F.; Hollingsworth, J. A.; Klimov, V. I.; Htoon, H. Near-Unity Quantum Yields of Biexciton Emission from CdSe/CdS Nanocrystals Measured Using Single-Particle Spectroscopy. *Phys. Rev. Lett.* **2011**, *106*, 187401/1−4.

(21) Mangum, B. D.; Sampat, S.; Ghosh, Y.; Hollingsworth, J. A.; Htoon, H.; Malko, A. V. Influence of the Core Size on Biexciton Quantum Yield of Giant CdSe/CdS Nanocrystals. *Nanoscale* **2014**, *6*, 3712−3720.

(22) Park, Y.-S.; Bae, W. K.; Pietryga, J. M.; Klimov, V. I. Auger Recombination of Biexcitons and Negative and Positive Trions in Individual Quantum Dots. *ACS Nano* **2014**, *8*, 7288−7296.

(23) Sampat, S.; Karan, N. S.; Guo, T.; Htoon, H.; Hollingsworth, J. A.; Malko, A. V. Multistate blinking and scaling of the recombination rates in individual silica-coated CdSe/CdS nanocrystals. *ACS Photonics* **2015**, *2*, 1505−1512.

(24) Mak, K. F.; He, K.; Lee, C.; Lee, G. H.; Hone, J.; Heinz, T. F.; Shan, J. Tightly bound trions in monolayer MoS_2. *Nat. Mater.* **2013**, *12*, 207−211.

(25) Gordon, J. M.; Gartstein, Y. N. Dielectric polarization, anisotropy and nonradiative energy transfer into nanometre-scale thin semiconducting films. *J. Phys.: Condens. Matter* **2013**, *25*, 425302.

(26) Roodenko, K.; Nguyen, H. M.; Caillard, L.; Radja, A.; Thissen, P.; Gordon, J. M.; Gartstein, Y. N.; Malko, A. V.; Chabal, Y. J. Anisotropic Optical Properties of Thin-Film Thiacarbocyanine Dye Aggregates. *J. Phys. Chem. C* **2013**, *117*, 20186−20192.

(27) Barnes, W. L. Fluorescence near interfaces: the role of photonic mode density. *J. Mod. Opt.* **1998**, *45*, 661−699.

(28) Novotny, L.; Hecht, B. *Principles of Nano-Optics*; Cambridge University Press: Cambridge, 2006.

(29) Chance, R. R.; Prock, A.; Silbey, R. In *Advances in Chemical Physics*, Vol. 37; Rice, S. A., Prigogine, I., Eds.; Wiley: New York, 1978; pp 1−65.

(30) Purcell, E. M. Spontaneous emission probabilities at radio frequencies. *Phys. Rev.* **1946**, *69*, 681.

(31) Kristensen, P. T.; Mortensen, J. E.; Lodahl, P.; Stobbe, S. Shell Theorem for Spontaneous Emission. *Phys. Rev. B: Condens. Matter Mater. Phys.* **2013**, *88*, 205308.

(32) Agranovich, V. M. In *Surface Polaritons*; Agranovich, V. M., Mills, D. L., Eds.; North Holland: Amsterdam, 1982; pp 187−238.

(33) Shen, C. C.; Hsu, Y. T.; Li, L. J.; Liu, H. L. Charge Dynamics and Electronic Structures of Monolayer MoS_2 Films Grown by Chemical Vapor Deposition. *Appl. Phys. Express* **2013**, *6*, 125801.

(34) Yim, C.; O'Brien, M.; McEvoy, N.; Winters, S.; Mirza, I.; Lunney, J. G.; Duesberg, G. S. Investigation of the optical properties of MoS_2 thin films using spectroscopic ellipsometry. *Appl. Phys. Lett.* **2014**, *104*, 103114.

(35) Rogach, A. L.; Klar, T. A.; Lupton, J. M.; Meijerink, A.; Feldman, J. Energy Transfer with Semiconductor Nanocrystals. *J. Mater. Chem.* **2009**, *19*, 1208−1221.